Chemical Science

ROYAL SOCIETY OF CHEMISTRY

EDGE ARTICLE

View Article Online
View Journal | View Issue

Cite this: *Chem. Sci.*, 2025, **16**, 16757

All publication charges for this article have been paid for by the Royal Society of Chemistry

Bio-inspired ion channels for suppressing interfacial parasitic reactions and enabling low-energy ion desolvation in aqueous supercapacitors

Yuting He,†[a] Jiangbin Deng,†[ab] Kaixin Wang,†[a] Qianzhi Gou,[a] Haoran Luo,[a] Ziga Luogu,[a] Zhaoyu Chen,[a] Ke Wen,[a] Yujie Zheng *[a] and Meng Li *[a]

The sluggish de-solvation reaction kinetics of hydrated ions and the occurrence of undesired water electrolysis on the electrode–electrolyte interface pose significant challenges to the practical deployment of aqueous supercapacitors. Interestingly, biological ion channels exhibit remarkable abilities to facilitate the de-solvation and low-energy transport of hydrated ions, and these are achieved through their size-limited confinement effects and electrostatic interactions. Inspired by such transit mechanisms of ion channels, we propose an interesting strategy to facilitate the rapid desolvation of electrode surface ions with low-energy transport. This strategy utilizes the aperture confinement effect and charge effect of biological ion channels to construct porous carbon electrodes. Concretely, we systematically reveal the relationship between the aperture size of the carbon electrode and ion migration rate, thereby obtaining the optimal channel radius (10 Å). To verify the modulation mechanism of the charge effect, four functional groups were sequentially incorporated into the carbon-based electrode, and it was determined that the –COOH group exhibited the optimal effect for accelerating the ion migration kinetics and restricting parasitic reactions. This modification destabilized the hydration shell of potassium ions, decreasing their average coordination number (ACN) from 6.0 to 2.1, thereby enabling the establishment of a low-resistance ion transport pathway. Concurrently, it achieved a fourfold enhancement in potassium ion permeation while significantly inhibiting the HER. This bio-inspired approach provides a new paradigm for designing high-performance aqueous energy storage systems through rational control of ion transport behavior on a molecular scale.

Received 6th July 2025
Accepted 6th August 2025

DOI: 10.1039/d5sc04992j

rsc.li/chemical-science

Introduction

Aqueous supercapacitors (SCs) have emerged as a promising energy storage technology due to their inherent safety,[1,2] low cost,[3,4] and high ionic conductivity of water-based electrolytes.[5–7] However, the practical application of these devices is fundamentally limited by the narrow electrochemical stability window (ESW) of aqueous systems,[8,9] which arises from two interrelated challenges.[10,11] First, the thermodynamic water decomposition potential of 1.23 V (theoretical) imposes a strict upper voltage limit, beyond which solvated water molecules in cation coordination spheres preferentially undergo reduction to generate parasitic hydrogen evolution at the electrode–electrolyte interface. Second, the formation of ordered solvation structures between metal cations and water molecules creates substantial hydration shells that increase the ionic radius and interfacial charge transfer resistance, significantly impeding mass transport kinetics while simultaneously promoting undesirable side reactions. These solvation-mediated phenomena, encompassing electrochemical instability and sluggish ion transport, collectively constrain the energy density and cycling stability of aqueous SCs, highlighting the critical need for innovative engineering strategies to modulate interfacial stability and overcome these intrinsic limitations.[12,13]

To avoid the hydrogen evolution reaction (HER) of solvent-tising water molecules, numerous strategies have been proposed, including the introduction of highly concentrated ligands to form a competitive coordination mechanism with solvated water molecules.[14,15] Other reported strategies include the establishment of a solid–liquid interface that serves as a protective layer to prevent direct contact between water molecules and the electrode,[16,17] and enhancing the HER inertness of electrodes.[18,19] Notably, electrolyte engineering is the most popular method to boost the cell voltage of aqueous SCs, and a representative example is the water-in-salt

[a]*National Innovation Center for Industry-Education Integration of Energy Storage Technology, MOE Key Laboratory of Low-grade Energy Utilization Technologies and Systems, CQU-NUS Renewable Energy Materials & Devices Joint Laboratory, College of Energy & Power Engineering, Chongqing University, Chongqing 400044, China. E-mail: limeng@cqu.edu.cn; zhengyujie@cqu.edu.cn*

[b]*School of Mechanical & Electrical Engineering, Yunnan Vocational Institute of Energy Technology, Qujing, Yunnan 655001, China*

† These authors contributed equally to this work.

electrolyte. In 2016, Suo *et al.* first reported the concept of the water-in-salt electrolyte, which is composed of 21 m LiTFSI solute salt and traces water solution.[20] In this scenario, water-induced parasitic reactions are significantly restricted, thereby boosting the cell voltage of aqueous lithium-ion batteries (LIBs).[14] However, the practical application of these electrolytes is hindered by their high cost, elevated viscosity, and significant mass transfer resistance. Thus, enhancing the cell voltage of aqueous SCs through electrode optimization remains an effective strategy.[21,22]

For instance, Liu *et al.* proposed an artificial coating layer consisting of NaX zeolite and NaOH-neutralized perfluoro sulfonic acid polymer. Molecular sieve channels and ion domains act together on molecular sieve components to repel solvated water molecules near Na^+, thereby inhibiting solvated water-induced side reactions.[23] Moreover, Zhou *et al.* used nitrogen (N)-doped graphene oxide (NGO) to construct an artificial interfacial film, which effectively suppressed the HER.[24]

Although designing electrode structures can effectively induce ionic desolvation, the persistent presence of solvation shells during ion transport across protective layers inevitably introduces kinetic energy loss at the electrode interface. This phenomenon hinders ion migration rates and also causes undesirable energy dissipation, ultimately compromising the high power density advantage of capacitors.

Interestingly, we found that biological ion channels enable the rapid transport and efficient desolvation of ions (*e.g.*, potassium ion channels can transport potassium ions at 10^8/s), and that the entire process is carried out with very low-energy consumption (mass transfer). These two features of low-energy desolvation and fast mass transfer are highly desirable for designing efficient aqueous supercapacitors. After studying a typical potassium channel of *Streptomyces mycoides*, we found that the channel is composed of a selective filter with domain-limiting and electrostatic effects, where the domain-limiting effect is realized by the narrow size (0.4 nm), and the electrostatic effect is realized by the interaction of amino acid groups with potassium ions (Fig. 1a). We speculate that it is the size-limiting effects and electrostatic interactions that allow for low-energy desolvation and rapid ion transport.

In a previous study, we prepared Meso-18C bionic electrodes. Meso-18C effectively removes the solvated shells of ions. This work focuses on the effective removal of the electrode material for the solvated structure of ions and the inhibition of the decomposition of water.[25–27] Previous work focused primarily on enhancing the de-solvation behaviour through pore size-limited domain effects and verified this approach, but did not thoroughly investigate the interactions between ions and charged groups. Therefore, in this work, a large number of simulation forms and methods were applied to monitor the transport behaviour of ions in the pore channels. The unique mechanism of interactions between ions and functional groups in the pore channels was verified through multi-dimensional simulation, combined with the electrochemical quartz crystal microbalance (EQCM) technique.[28] This work addresses the knowledge gaps in theoretical studies on the influence of functional groups on ion transport behaviour under domain-limited conditions, providing additional insights and ideas.[29–31]

Inspired by the rapid ion transport and de-solvation mechanisms in biological ion channels, we investigated the interaction between hydrated ions and functional groups under pore size-limited conditions, as well as the ionic de-solvation process (Fig. 1a). Through simulations, we identified the optimal pore size for desolvation and the functional group with the strongest desolvation effect. Subsequently, sub-nanometer-scale ion channels were constructed on the electrode surface using soft and hard templates, followed by carboxyl group modification to align with the simulation results (Fig. 1b).[32–35]

Experimental analysis revealed that this approach reduced the average coordination number (ACN) of water molecules around potassium ions from 6.0 to 2.1, while a low-resistance ion transport pathway was gradually formed within the channel. Notably, this design not only significantly suppressed the HER but also resulted in a fourfold increase in the number of potassium ions entering the pore channel. Our work yields more in-depth insights into how modified charged groups influence ion transport behavior within nanoscale pores, while offering novel perspectives on ion-charge interactions under pore-confined conditions.

Results and discussion

First, the critical role of the aperture size of ion channels during the de-solvation process was investigated.[36] Ion channels of different sizes (8 Å, 9.6 Å, 10 Å, 12 Å, 20 Å, and 30 Å) were simulated, as shown in Fig. S1a. By comparing and analyzing the number of K^+ entering the channel (Fig. S1b), the statistical results showed that no K^+ entered the ion channel with a pore size of 8 Å; a higher number of potassium ions entered the ion channels of 20 Å and 30 Å. Compared to the smaller pore sizes of 9.6 Å and 12 Å, the number of K^+ entering the 10 Å ion channel was significantly higher.

To verify the de-solvation effect of the different pore sizes, the ratio of the number of water molecules to K^+ was determined, and the results showed that the lowest water-to-potassium ratio was exhibited by the 10 Å ion channel, which also showed the strongest de-solvation effect (Fig. S1c).[37] Fig. S2 shows the effect of introducing functional groups on de-solvation, based on pore size-dependent de-solvation in biomimetic ion channels (10 Å and 12 Å), using the carbonyl group with size 2 Å as an example. The 12 Å of the biomimetic ion channel allowed the greatest number of potassium ions to enter, and showed the lowest water-to-potassium ratio. Therefore, the ion channel with a pore size of 10 Å is expected to provide the most optimal de-solvation performance among the pore sizes studied after functional group modification.

By introducing electronegative functional groups, we aim to facilitate the detachment of cations from the solvation shell through electrostatic interactions and synergistic hydrogen bonding, where these groups act as donors and acceptors. These specific interactions are designed to effectively mitigate the de-solvation energy barrier, ultimately leading to a significant enhancement in cation migration.[38,39] Therefore, several

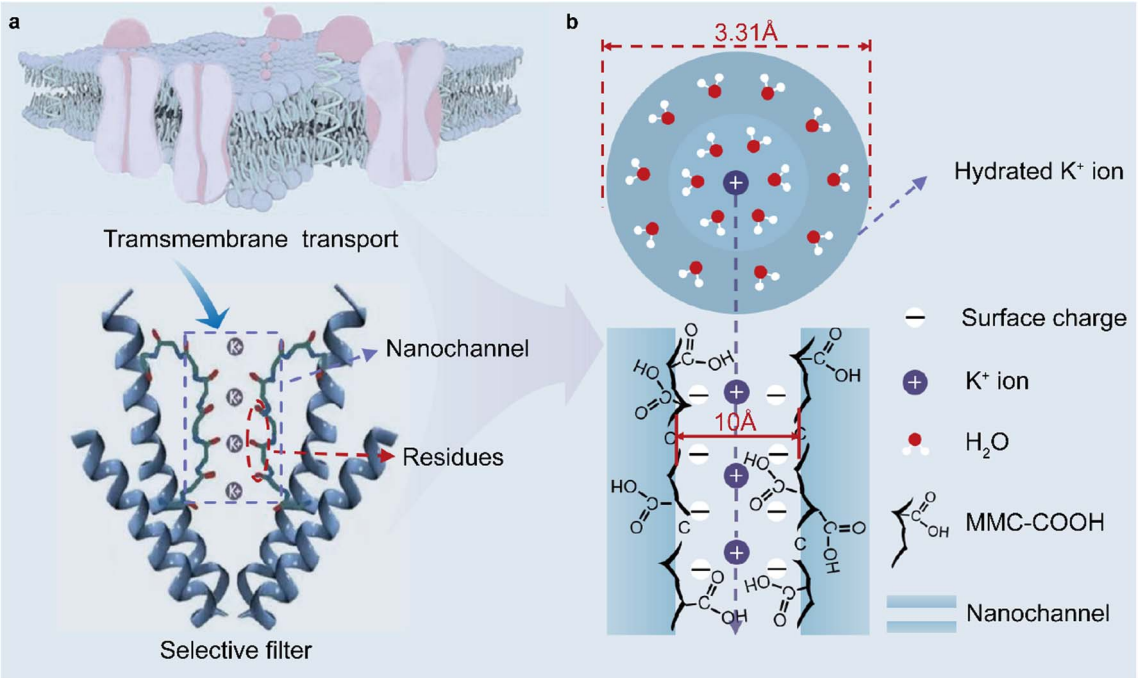

Fig. 1 Schematic structure of a bio-inspired channel. (a) De-solvation mechanism of a biological membrane. (b) Bio-inspired channels constructed based on the de-solvation mechanism of biological ion channels.

common electronegative functional groups (–NH_2, –CO, –OH, –COOH) were chosen for the construction of biomimetic ion channels to study their effects on de-solvation. Molecular dynamics (MD) simulations were used to visually explore the effects of different functional group modifications on desolvation.[40,41] The constructed models are shown in Fig. 2a, and –COOH is used as an example here.

Fig. 2b summarizes the adsorption energies between the different functional groups and K^+ and H_2O, and $E_{ad}(K^+)$ is larger than $E_{ad}(H_2O)$ on all functional group substrates. The –CO functional group has the highest adsorption energy for K^+, which reached 1.36 eV, followed by –COOH, which has an adsorption energy of 1.34 eV for K^+. Additionally, the highest adsorption energy for H_2O was exhibited by –COOH, which reached 0.66 eV, indicating that it is favorable for inducing the ions to de-solvate the solvated shells. These results indicate that the introduction of carboxyl groups into the biomimetic ion channel is expected to achieve desolvation by utilizing a variety of interaction forces, such as electrostatic forces, hydrogen-bonding forces, and van der Waals forces, and can effectively improve the transport rate of K^+.[44,45]

Bio-inspired ion channels for mesoporous and microporous carbon (MMC), MMC-NH_2, MMC-CO, and MMC-OH were constructed, as shown in Fig. S3. In the solution region away from the interface, K^+ usually forms a coordination compound with six water molecules.[28] However, once it enters the negative region, the number of coordination sites with water molecules significantly decreases. To quantify this phenomenon, the radial distribution function (RDF) and the ACN of K^+–O (H_2O) were counted. The models were divided into three regions along the *y*-axis: 30–92 Å (negative region), 208–270 Å (positive region), and the solution region (rest). The statistical results show that carboxyl-modified cations have the fewest surrounding water molecules in the negative region. Furthermore, the CN integral curve indicates that, in the anode region of the carboxyl-modified ion channels, each cation contains an average of 2.6 fewer solvated water molecules (ligands) compared to the unmodified channel.

The anode region facilitated the de-solvation of K^+ to some extent by exploiting the pore domain confinement effect, and the anode region also significantly enhanced the desolvation through the synergistic effect of the pore domain confinement and charge effects (Fig. S4).[27] As depicted in Fig. 2c, the first solvation sheath of K^+ remained nearly unchanged in MMC-NH_2 and MMC-OH, and there was little decrease in the number of water molecules around the cation. However, the peaks in MMC-COOH appeared to be significantly reduced, and the number of water molecules around the potassium ions was significantly reduced in the first and second solvation sheaths. Because water molecules are proton donors for the HER, a decrease in their number will directly lead to a decrease in proton donors, thus reducing the frequency of the HER.[46]

In addition, the number of K^+ in the channel and the water-potassium ratio were determined to verify the de-solvation effect (Fig. 2d). In the MMC, the number of incoming K^+ was only 15.73, while the water-potassium ratio was as high as 110.29. In contrast, the highest number of incoming K^+ was found in MMC-OH, which reached 44.65, followed by MMC-COOH, which was 43.99, and the lowest water-potassium ratio was found in MMC-COOH, which was only 35.26. The significantly reduced number of water molecules in the channel and a higher potassium ion concentration in the negative region of

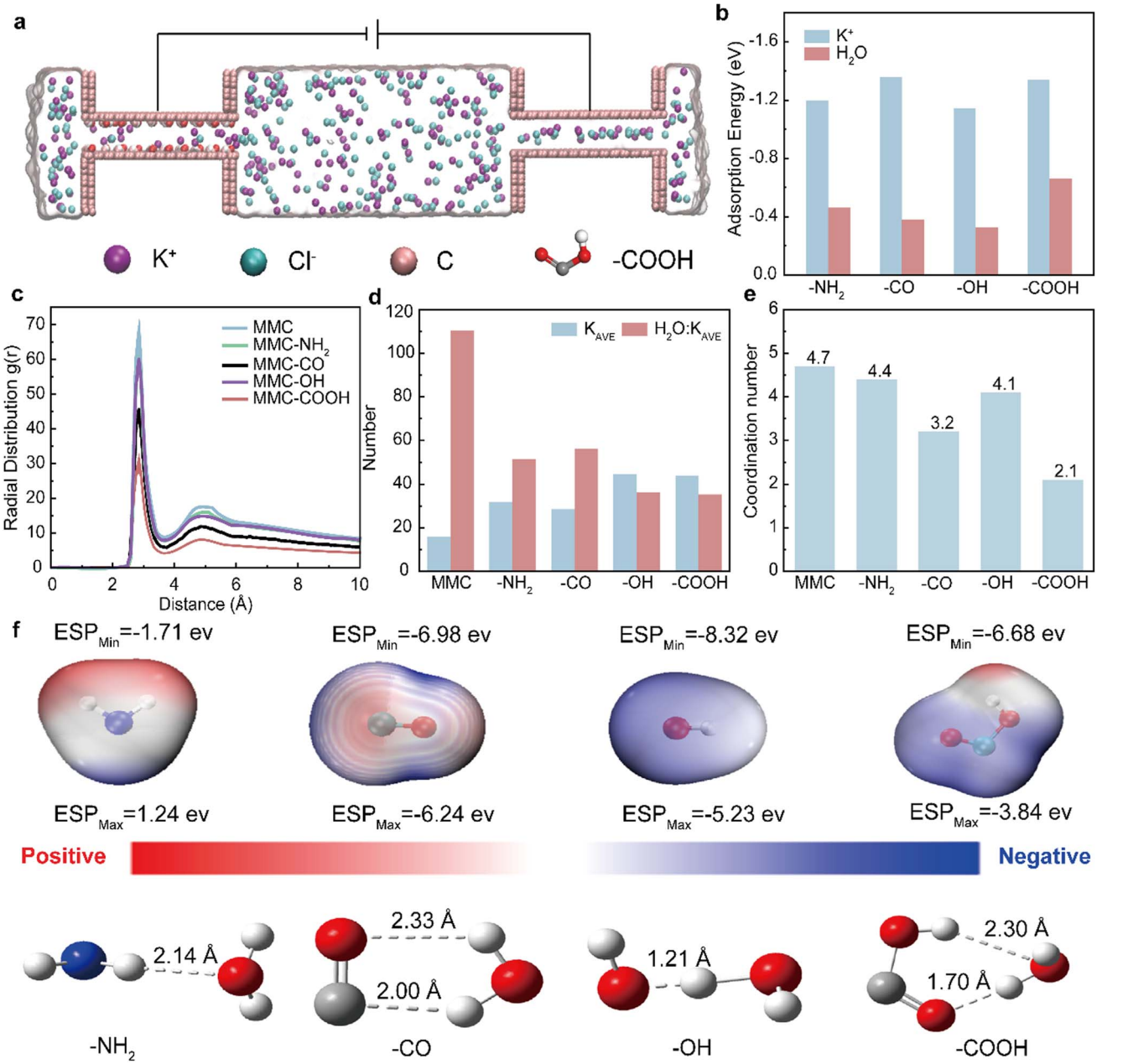

Fig. 2 Probing the effect of bionic ion channels modified with different functional groups on cation de-solvation. (a) Snapshots of an MD model of biomimetic ion channels. (b) Adsorption energies of K^+ and H_2O with different functional groups. (c) Number of potassium ions and water-potassium ratio statistics in the negative channel. (d) Radial distribution function (RDF) within the negative channel. (e) ACN of cations within the negative channel. (f) Distribution of the electrostatic potential values of different groups.

MMC-COOH are favorable for enhancing the ion adsorption and desorption processes. Indeed, according to the ACN results, MMC reduced the average water molecule coordination number from 6 to 4.7, demonstrating the de-solvation effect of the pore size-limited region (Fig. 2e).

Under the synergistic effect of the pore size-limited domain and the charge effect, the de-solvation performance of MMC-NH_2 is suboptimal. Its coordination number is reduced by only 0.3. In contrast, MMC-COOH demonstrates the strongest de-solvation performance. It reduced the average water molecule coordination number of K^+ from 6 to 2.1. This significantly decreases the number of solvated water molecules in the negative electrode region, thereby reducing the likelihood of the HER through the reduction reaction between water molecules and the electrode surface.[47,48]

Density functional theory (DFT) was applied for structural optimization, and the results are summarized in Fig. 2f.[42] The largest negative electrostatic potential was exhibited by the hydroxyl group (–OH), while the amino group (–NH_2) exhibited the smallest negative electrostatic potential, and the group with negative electrostatic potential can interact with the cation to compensate for the de-solvation energy barrier, thus facilitating

the desolvation and migration of the cation.[43] Then, the number of hydrogen bonds formed by different functional groups with water molecules was also confirmed. Both carbonyl (–CO) and carboxyl (–COOH) groups can form hydrogen bonds with water molecules, and the hydrogen bond between the carboxyl group and water molecule (–COOH–H_2O) is shorter and more stable than that of –CO, making it less prone to dissociation. Therefore, –COOH is more conducive to interacting with water molecules to achieve desolvation. The possibility of the release of hydrogen as a result of the reduction reaction between water molecules and the electrode surface is greatly decreased (Table S1).

A typical ordered mesoporous silica (SBA-15) template method was used to prepare mesoporous carbon at the nanometer scale, which was carboxylated to obtain MMC-COOH (Fig. 3a). Our calculation results were experimentally verified, and the carboxyl functional group with the best dissolution effect was used to synthesize carbon-based electrodes. MMC and MMC-COOH were synthesized according to previous studies.[49] To quantify the pore structure of the prepared samples, nitrogen sorption–desorption tests were performed. As shown in Fig. S5, these results show a narrow and approximately parallel hysteresis loop between relative pressures of 0.4–1.0, indicating that the material possesses typical microporous properties. The pore size of the prepared MMC was further quantified using non-local density functional theory (NLDFT), and it was determined to be concentrated around 1 nm, as shown in Fig. 3b, which is consistent with the pore size results from the simulation screening.

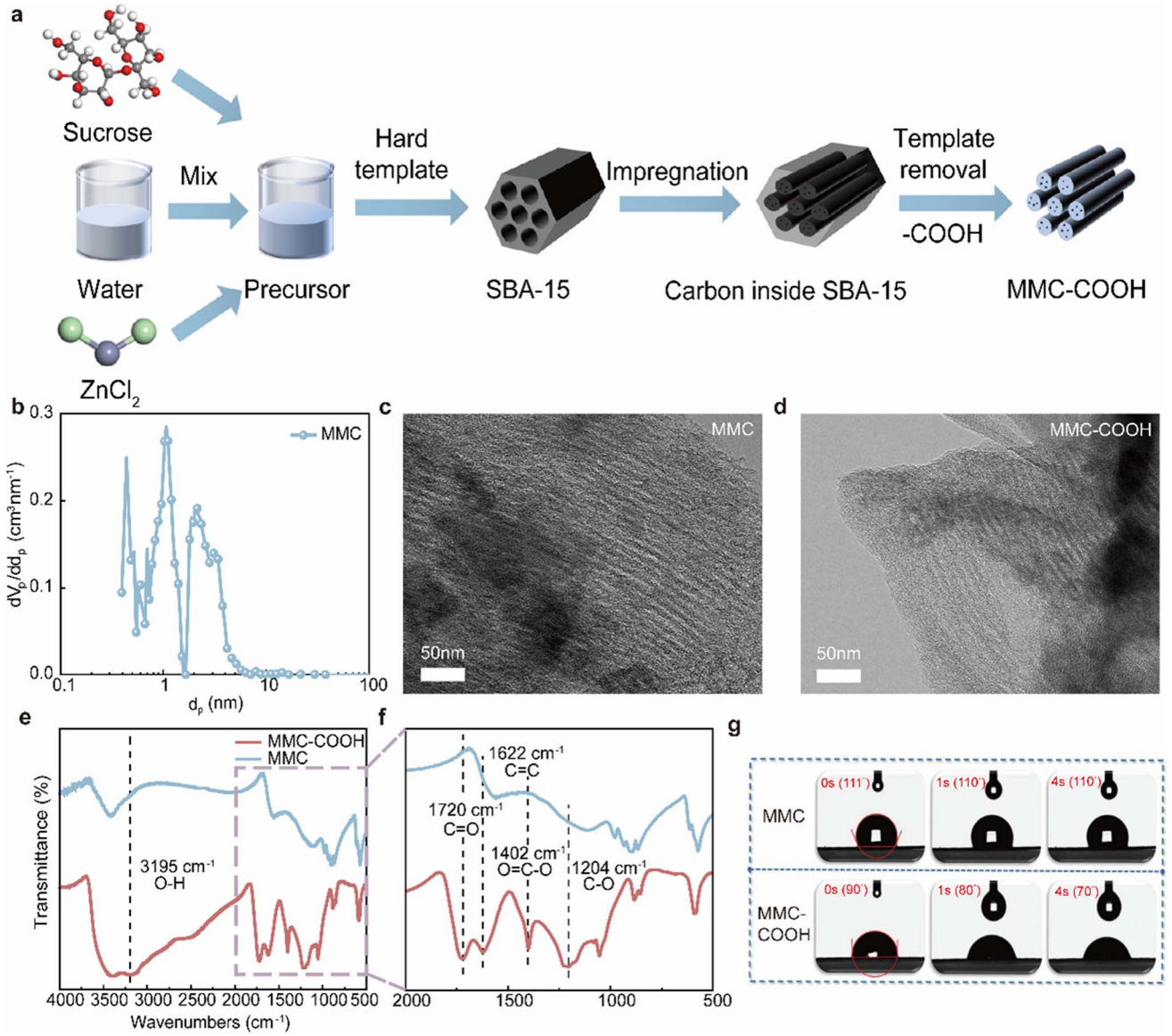

Fig. 3 Preparation and characterization of electrode materials. (a) Schematic diagram of the electrode material preparation process. (b) Pore size distribution diagram. (c) TEM image of MMC. (d) TEM image of MMC-COOH. (e) FTIR spectrum of the O–H bond-bending vibration. (f) Localized magnification of the FTIR spectrum. (g) Contact angle test plots of MMC and MMC-COOH.

Although the disorder of the MMC-COOH samples slightly increased during the modification process due to multiple stirring and other reaction factors, the ordered micropore structure remained consistent. This phenomenon was first observed in the scanning electron microscopy (SEM) images (Fig. S6a and b). Transmission electron microscopy (TEM) images further confirmed the nanoporous morphology of MMC and MMC-COOH (Fig. 3c and d). The morphological characterization results proved that successful preparation of ordered mesoporous carbon occurred, and the morphology was unchanged after modification of the carboxyl groups. The corresponding energy dispersive X-ray spectroscopy (EDS) elemental mapping of the TEM images showed the uniform distribution of C and O in the MMC-COOH samples (Fig. S6c and d), which proved that successful modification of the carboxyl groups occurred.

The structure of MMC-COOH was characterized by Fourier transform infrared (FTIR) spectroscopy, and the FTIR spectra at 3195 cm^{-1} confirmed the formation of O–H stretching vibrations in MMC-COOH (Fig. 3e), with bending vibration peaks at 1204, 1402, 1622, and 1720 cm^{-1} (Fig. 3f), and the appearance of these peaks indicates the presence of carboxyl groups in MMC-COOH. In addition, the contact angle gradually decreased with the introduction of carboxyl groups (Fig. 3g), and after 4 s, the contact angle of MMC-COOH was 70°, which was much smaller than that of MMC (110°), indicating that there was increased wettability of the electrolyte at the interface of the negative electrode.[38] This phenomenon may be ascribed to the –COOH group, which can promote the synergistic action of the hydrogen bond acceptor and donor, and interact with water molecules to achieve efficient desolvation through the formation of strong hydrogen bonds with H_2O.

Based on the aforesaid analysis, it can be concluded that modification of the carboxyl groups on MMC successfully occurred, and then MD simulations were applied to investigate the effects of this modification strategy on the ion migration process. The effect of the modified functionalized groups on the water distribution is shown in Fig. 4a.[50] It was found that the water molecules in the electrical double-layer (EDL) entered the biomimetic ion channel under the voltage drive, and the number density distribution of the water molecules in the MMC-COOH showed a gradual decreasing tendency, which was much lower than that of the water molecules in the MMC.

The quantity density distribution of K^+ in MMC and MMC-COOH was determined to be 0.022 (Fig. 4b), which was much higher than that of MMC, at 0.006. This is because electronegative groups attract cations *via* electrostatic and hydrogen-bond interactions.[43] It was further demonstrated that the carboxyl group enhanced the migration kinetics of K^+ at the interface, and the accumulation of K^+ at the electrode interface was expected to enhance the adsorption and desorption at the interface, thus improving the overall energy density and power density of the SC. Fig. 4c exhibits the de-solvation process and K^+ migration behavior of MMC-COOH upon ion adsorption. The introduction of carboxyl groups into MMC effectively desolvates the solvated water molecules and prevents the entry of free water molecules by adsorbing and immobilizing solvated water molecules through electrostatic and hydrogen-bonding interactions.

In addition, EQCM is an effective operational technique for monitoring the ion flux at the polarized electrode interface. Fig. S7a and c display the cycling reversibility of the MMC-COOH and MMC materials, with satisfactory reversibility for both materials. In the current profile variation plots (Fig. S7b and d), these two materials exhibit a clear difference in the current peaks. The MMC-COOH material exhibits larger current fluctuations and higher peaks. This suggests that modification of this group enhances the kinetic rate of the electrochemical reaction at the electrode, promotes the adsorption and desorption of more ions, and consequently demonstrates a larger peak current and a larger closure area. In contrast, the MMC materials demonstrated smaller current fluctuations and lower peaks, indicating a relatively slow dynamic response.

To further investigate the ion dehydration mechanism during cation adsorption, the electrode mass change (Δm) and cumulative charge (ΔQ) induced by electrochemical ion adsorption/desorption in carbon electrodes were calculated according to the Sauerbrey equation, and $\Delta m - \Delta Q$ plots were linearly fitted (Fig. 4d).[51] These results show that Δm increases for both materials with the accumulation of cathodic charge, indicating the existence of a cation adsorption mechanism on the electrode surface.

The changes in the solvation shell of hydrated ions were further investigated by quartz crystal microbalance (QCM) and cyclic voltammetry (CV). Calculated according to CV and quality change (Fig. 4e and S7e), and notably, when compared with the QCM curve of MMC, the QCM curve of MMC-COOH depicts an abnormal increase between −0.2 V and 0.2 V, which is due to the stripping of solvated water molecules upon entering the ion channel,[3] whereas an abnormal decrease located between −0.5 V and −0.3 V indicates that some solvated water molecules interact with the carboxyl groups and remain in the ion channel. Fig. 4f shows the evolution of the solvated shell during the desorption of K^+ from the MMC-COOH surface. When K^+ undergoes voltage-driven desorption behavior, some solvated water molecules interact with the groups to form strong hydrogen bonds. This process significantly affects the distribution of interfacial water molecules and their activity, reduces the interaction of K^+ with water molecules during transport, and lowers the resistance to ion migration.

As depicted in Fig. 4g and h, the potential of the mean force (PMF) was used to study the change in the magnitude of the free energy during cation migration.[50] The comparative results show that with the adsorption and desorption processes, the water molecules in MMC continued to accumulate, leading to a gradual increase in the free energy of K^+. In contrast, in MMC-COOH, there is a large free energy at 0 ps for potassium ions due to the removal of solvated water molecules aggregated at the interface; at 2000 ps, the free energy of potassium ions tends to zero. This phenomenon is due to the fact that many solvated water molecules, driven by an electric field, reconfigure hydrogen-bond networks, with most of them forming ion channels with specific structures. This significantly reduces the activity of solvated water molecules, compensates for the

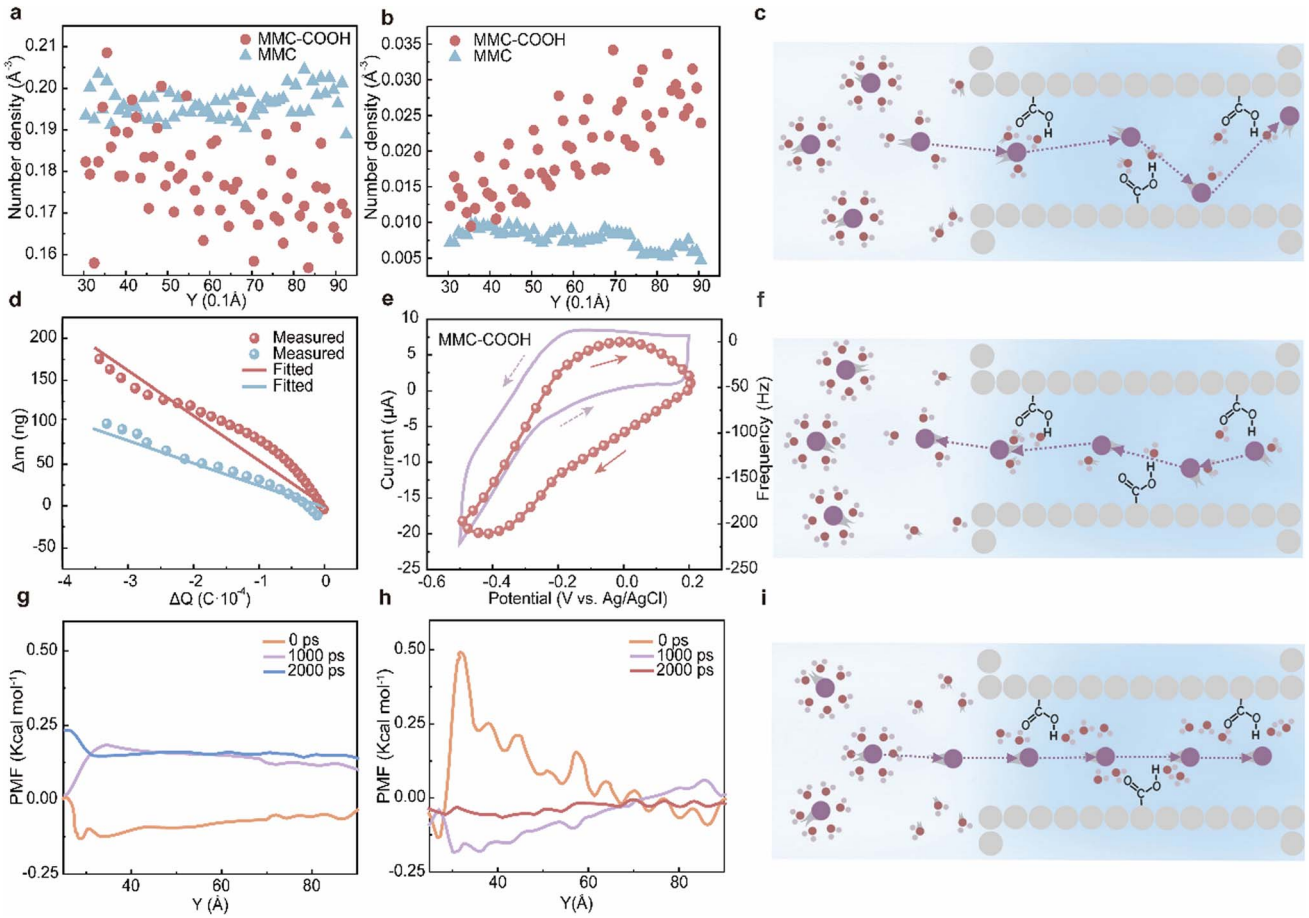

Fig. 4 Effect of desolvation on hydrogen bonding and kinetics. (a) H_2O number density within the ion channel. (b) K^+ number density within the ion channel. (c) Schematic diagram of the K^+ adsorption process. (d) $\Delta m - \Delta Q$ curves of MMC and MMC-COOH. (e) EQCM of MMC-COOH. (f) Schematic diagram of the K^+ desorption process. (g) PMF of K^+ in MMC at different times. (h) PMF of K^+ in MMC-COOH at different times. (i) Schematic diagram of K^+ superfluid transport.

dissolving energy barrier of K^+, improves the transport rate of potassium ions, and contributes to the superfluid transport of K^+ (Fig. 4i).[28] This also implies that the electric field distribution inside the electrode is uniform, and the entire system is in a low energy and stable state, which supports efficient ion transport and energy storage. Thus, the experimental and simulation results validate the successful preparation of the biomimetic ion channel and its potential to enhance electrochemical performance.

In addition, *ab initio* molecular dynamics (AIMD) simulation was used to study the behavior of hydrated ions at the interface.[42] As shown in Fig. S8, the solvation effect on MMC gradually drives the hydrated K^+ away from the negative interface. However, on the MMC-COOH substrate, the solvated shell of the hydrated K^+ is distorted and disrupted by the electrostatic interactions of the carboxylate groups, and the contact between K^+ and the negative electrode surface is induced, thereby enhancing charge transfer. To investigate the interfacial hydrogen-bonding behavior, the number of water molecules and the total number of hydrogen bonds within the negative electrode interface were counted (Fig. S9). Compared to MMC, the number of water molecules in the ion channels modified with the different groups decreased, and the number of hydrogen bonds should have shown a similar trend, although this was not the case. The carbonyl and carboxyl groups formed new hydrogen bonds with solvated water molecules, increasing the overall number of hydrogen bonds.

The presence of –COOH resulted in the introduction of new hydrogen bond donors and acceptors, leading to recombination of the existing hydrogen-bond networks in a limited space (Fig. 5a). The statistics of the numbers of strong and weak hydrogen bonds are shown in Fig. 5b. The decrease in the number of weak hydrogen bonds follows a trend that mirrors the reduction in the number of water molecules at the negative interface. Similarly, the trend of strong hydrogen bonds correlates with the overall trend in the total number of hydrogen bonds. This can be attributed to the fact that hydrogen bonds between water molecules are generally weak, whereas those formed between water molecules and radicals are stronger—with the same mechanism explaining why hydrogen bonds between water molecules and functional groups are stronger than those between water molecules themselves.

Strong hydrogen bonds are conducive to the inhibition of the activity of solvated water molecules and significantly reduce the

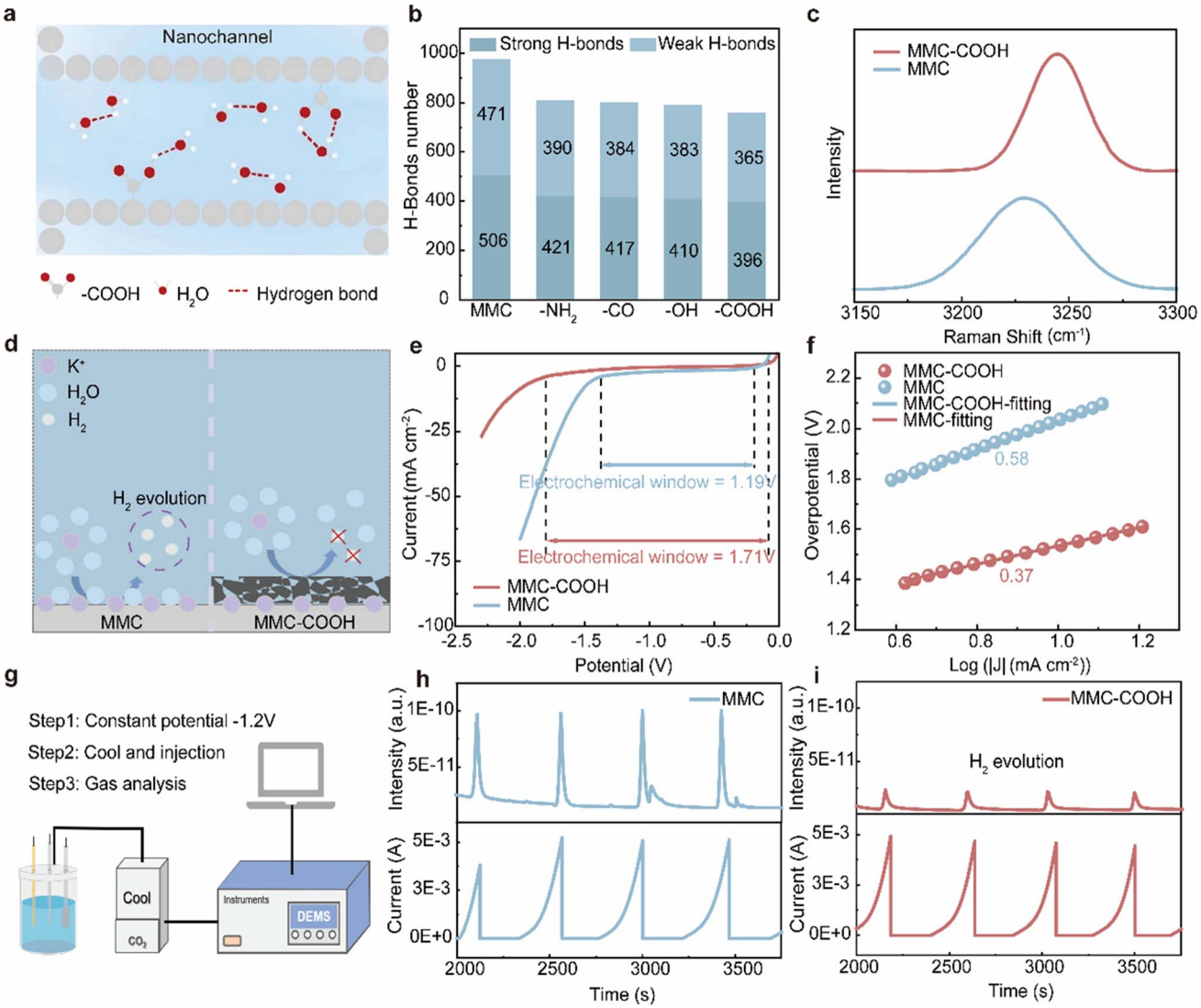

Fig. 5 Hydrogen-bonding network reconfiguration and hydrogen precipitation inhibition. (a) Schematic diagram of hydrogen-bond structure changes in ion channels. (b) Statistics of the number of strong and weak hydrogen bonds within the bionic ion channel. (c) Raman spectra of O–H bonds of water molecules. (d) Diagram of the interface hydrogen evolution effect. (e) LSV curves. (f) Tafel curves. (g) Schematic diagram showing *in situ* DEMS equipment set-up. (h) DEMS of MMC. (i) DEMS of MMC-COOH.

likelihood of water decomposition. The Raman test further characterized the O–H bond between the water molecules, and showed that the stronger peak at approximately 3230 cm^{-1} corresponded to the hydrogen bond in the water molecules.[52] Fig. 5c shows that the intensity of the strong peak in MMC-COOH was enhanced and blueshifted compared to that in MMC, and the modification of the carboxyl group caused the peak to shift from 3229 cm^{-1} to the high wavelength of 3244 cm^{-1}. This suggests that the O–H bond between water molecules is a strong hydrogen bond, while the formation of strong hydrogen bonds between water molecules and radicals is beneficial for inhibiting the activity of solvated water molecules. This indicates that the strength of the O–H bond between water molecules has increased, and the activity of water molecules has effectively been inhibited.

The narrowing of the peak spread indicates that the O–H bond in the water molecule is transformed into a hydrogen bond between the water molecule and the carboxyl group. This confirms that the modification of the carboxyl group realizes the reconfiguration of the hydrogen-bonding network, and the structure of the water molecule can be transformed from a diversified hydrogen-bonding network to an arrangement with greater homogeneity. This homogeneous hydrogen-bonding network increases interfacial stability, reduces side reactions, and promotes charge transfer, thereby significantly enhancing the overall system stability.

Collectively, Fig. 5d illustrates the effect of MMC-COOH on hydrogen evolution by design. This is further confirmed by the linear sweep voltammetry (LSV) curve in Fig. 5e, where the hydrogen precipitation onset potential of MMC was obtained as 1.19 V by LSV, and the delayed hydrogen evolution starting

potential after the introduction of the carboxylate group was 1.71 V, which indicated that the modification of the carboxylate group significantly increased the hydrolysis onset potential. The Tafel curves exhibited in Fig. 5f show a Tafel slope of only 0.37 for MMC-COOH, while that of MMC is 0.58. There is a lower Tafel slope and overpotential for MMC-COOH, and the lower overpotential decreases the occurrence of side reactions and increases the lifetime and stability of the electrode.

The higher hydrogen precipitation onset potential indicates that the carboxylate group modification can effectively inhibit the hydrogen precipitation reaction and increase the stability and efficiency of the electrode. Dynamic monitoring of H_2 evolution in the system was performed using *in situ* differential electrochemical mass spectrometry (DEMS) because it enabled spontaneous gas evolution to be observed during the standby cycle (Fig. 5g).[23] Fig. 5h and i display the precipitation of hydrogen from MMC and MMC-COOH during several electrochemical cycles. A clear hydrogen precipitation peak was observed for MMC during charging and discharging, while the hydrogen precipitation peak of MMC-COOH was weaker. This phenomenon indicates that MMC-COOH effectively inhibited hydrogen precipitation.

The effect of MMC-COOH on the performance of carbon wall SCs was systematically investigated. First, DFT simulations were used to analyze the electronic structure and charge distribution of the modified carbonylated carbon walls (MMC-COOH). Their structures are shown in Fig. S10a–c. Notably, the yellow region indicates the charge aggregation region, and the blue region indicates the charge dissipation region (Fig. S10d). Compared with MMC, MMC has fewer charge aggregation regions and a relatively dispersed charge distribution.

After the introduction of carboxyl groups (–COOH), charge rearrangement occurs on the porous carbon surface, and the carboxyl groups induce the formation of a significant electron accumulation region around them, which increases the charge density in this region (Fig. S10e and 6a). The long and complex charge transfer pathways in porous carbon materials lead to low charge transfer rates, while the carboxyl groups provide new charge transfer pathways that facilitate the transfer of electrons towards the carboxyl region, thus increasing the overall charge transfer efficiency of the materials. The electron localization density as a function of the plots of MMC *vs.* MMC-COOH again confirms this phenomenon. As shown in Fig. S10f, the electron density distribution on the MMC substrate is relatively uniform, and no significant electron accumulation was observed. In contrast, the introduced carboxyl group in MMC-COOH induces a significant accumulation of electrons in its neighboring region (red region).

The increase in electron localization density improves the electronic conduction capability of the material, which can enhance the overall electrochemical reaction rate. This charge rearrangement phenomenon was also confirmed in the density of states (DOS) (Fig. 6b), where MMC-COOH showed a higher electronic DOS, suggesting increased electrical conductivity of the modified carbon walls. The state densities of the elements in MMC-COOH were further analyzed, as shown in Fig. S11a. The carbon element in the carboxyl group contributes the most to the conductivity, followed by the oxygen element, and the hydrogen element in the carboxyl group contributes almost nothing to the conductivity. Based on the above results, the porous carbon material modified with carboxyl groups (MMC-COOH) showed higher electrical conductivity.

The impedance characteristics of the MMC and MMC-COOH electrode materials were further analyzed by electrochemical impedance spectroscopy (EIS) (Fig. 6c). MMC-COOH is characterized by a low contact resistance of 0.41 Ω, which is significantly lower than that of MMC (2.26 Ω). Fig. 6d indicates that the number density profile of potassium ions in MMC-COOH is relatively smooth at different *z*-axis positions, showing high number densities at certain positions, whereas the number density distribution in MMC fluctuates considerably, showing several peaks and troughs. The smooth profile of the number density suggests that in MMC-COOH, the diffusion resistance of potassium ions is reduced, enabling a more uniform distribution of K^+ across various positions. On the contrary, the significant fluctuation in number density in MMC materials indicates that the movement of potassium ions is subject to greater resistance. Moreover, the MMC-COOH electrode exhibited the electrochemical properties of lower charge transfer resistance and diffusion impedance as compared to MMC, which significantly increased the efficiency of charge transfer and ion diffusion.

Calculations based on the PMF (Fig. 6e) showed that the resistance of K^+ was abnormally high upon entering the aperture, a phenomenon that can be attributed to the fact that hydrated K^+ ions encounter great resistance because their hydration shells are distorted and aggregated outside the channel upon entering the biomimetic ion channel. However, once inside the ion channel, the resistance faced by K^+ is subsequently reduced due to the reduction in the number of solvated water molecules and the compensation of the desolvation energy barrier of the hydrated K^+ by the carboxyl group, which contributes to the rapid migration of the ions on the electrode surface (Fig. S11b).[38]

The mean square displacement (MSD) results (Fig. 6f) further indicate that the significant enhancement of the ionic MSD of MMC-COOH improves the migration kinetics of the ions, and these atomic-scale insights provide a guide for studying the electrochemical kinetics of K^+ SCs at the electrode interface. The experimental results fully demonstrated that carboxyl group modification can effectively improve the electrochemical performance of carbon-walled SCs. The charge–discharge (GCD) curves of MMC and MMC-COOH showed triangular shapes at a current density of 1 A g^{-1}, further demonstrating that these two materials are highly reversible and have desirable capacitive properties for SC applications (Fig. 6g).

The MMC-COOH electrode exhibited the highest specific capacitance of 128 F g^{-1} at the longest discharge time, while the specific capacitance of MMC was only 49 F g^{-1}. In addition, the integration area of the CV curve is larger for MMC-COOH, which is consistent with its superior capacity. Fig. 6h depicts the decrease in capacitance with the increasing current density that occurred. Even at a current density of 10 A g^{-1}, MMC-COOH

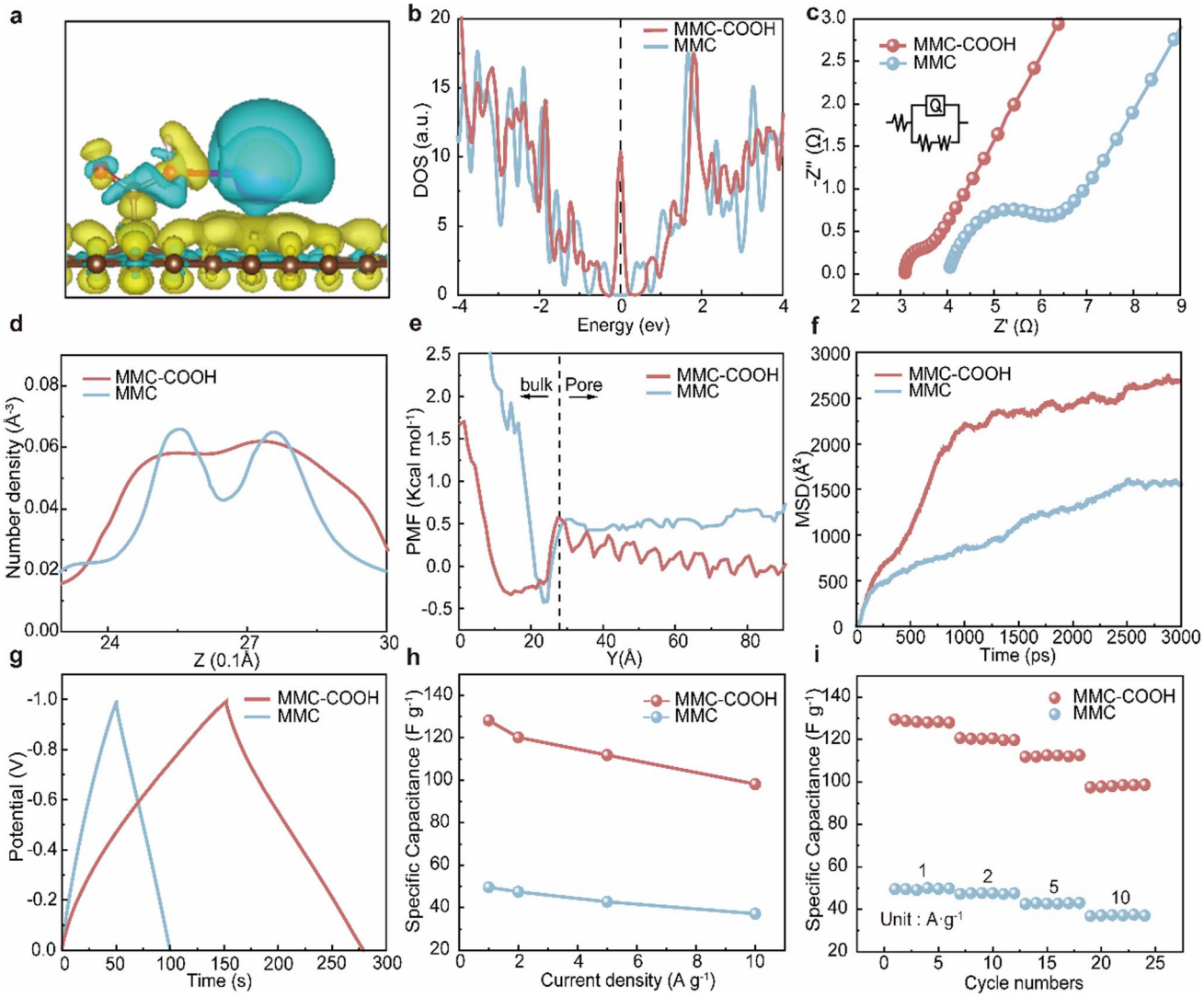

Fig. 6 Influence of diffusion kinetics and electrochemical properties. (a) Charge differential density of MMC-COOH (0.001(e Å^{-3})). (b) Density of states (DOS) of MMC and MMC-COOH. (c) EIS curves. (d) Number density plot of cations in the *Z* direction. (e) PMF of MMC and MMC-COOH. (f) MSD of K^+. (g) GCD curves of MMC and MMC-COOH at 1 A g^{-1}. (h) Comparison of the capacitance of MMC and MMC-COOH at different current densities. (i) Comparison of the rate performance of MMC and MM-COOH.

maintained a specific capacitance of 98 F g^{-1}, which is much higher than that of MMC at 1 A g^{-1}. Fig. 6i shows that the capacitance of MMC and MMC-COOH at different current densities decreases with increasing current density. At 10 A g^{-1}, the specific capacitance of MMC is only 37 F g^{-1}, which is much lower than that of MMC-COOH. This can be attributed to the improved conductivity and ionic transport of MMC-COOH due to the introduction of carboxyl groups on its surface, thus enabling it to maintain a satisfactory electrochemical performance at high current density. These results comparing the rate performance of MMC and MMC-COOH at different current densities show that MMC-COOH exhibits superior electrochemical properties at high current densities.

Finally, long cycle tests (under 5 A g^{-1}) of two samples are demonstrated in Fig. S12, where MMC-COOH showed superior cycle stability, demonstrating the long-term effectiveness of this electrode material for ion-accelerated desolvation. Ultimately, compared with other SCs (Fig. S13), our electrode demonstrates superior performance in both multiplicity and capacity, owing to the contributions of ion acceleration and desolvation, further highlighting the outstanding results of the present work.

Conclusion

In this study, we address the key factor limiting the application of aqueous SCs, *i.e.*, the solvation shell of interfacial ions, and propose to achieve efficient ion desolvation during transport through the construction of artificial ion channels. Our strategy employs the synergistic combination of size confinement and electrostatic effects to engineer porous carbon electrodes that enable rapid ion desolvation with low-energy transport. Additionally, a high-speed ion channel is formed during the

adsorption and desorption of K^+, which significantly boosts the ion transport rate and compensates for the kinetic loss associated with ion desolvation.

This design reduces the hydration shell of potassium ions, lowering their average coordination number from 6.0 to 2.1, while simultaneously establishing a low-resistance ion conduction pathway. The optimized electrode exhibits a four-fold enhancement in potassium ion flux with significantly inhibited hydrogen evolution. Compared to the existing 'water-in-salt' electrolyte strategy, our method not only effectively inhibits the HER but also enables rapid cation transport, overcoming several limitations inherent in traditional approaches. This study opens new research directions and development opportunities to address solvent stability challenges in other energy storage technologies, providing significant academic and practical value.

Author contributions

Y. H. conceived and designed the study. J. D. and K. W. conducted data curation and analysis, and wrote the original draft. Q. G. contributed to data curation. H. L., Z. L., Z. C., K. W., and M. L. provided resources and materials. Y. Z. participated in writing the original draft. M. L. acquired funding and supervised the research.

Conflicts of interest

The authors declare no conflicts of interest.

Data availability

The authors confirm that the data supporting the findings of this study are available within the article and its SI. See DOI: **https://doi.org/10.1039/d5sc04992j**.

Acknowledgements

This research was financially supported by research grants from the Natural Science Foundation of China (52173235), the Key Project of Chongqing Technology Innovation and Application Development Special Project (CSTB2025TIAD-KPX0020), the Hainan Province Science and Technology Special Fund (ZDYF2024SHFZ038), and the Venture & Innovation Support Program for Chongqing Overseas Returnees (CX2021018). We would like to thank the Analytical and Testing Center of Chongqing University for their support in materials characterizations.

References

1 S. Chen, M. Zhang, P. Zou, B. Sun and S. Tao, Historical development and novel concepts on electrolytes for aqueous rechargeable batteries, *Energy Environ. Sci.*, 2022, **15**(5), 1805–1839.

2 J. Xie, D. Lin, H. Lei, S. Wu, J. Li, W. Mai, P. Wang, G. Hong and W. Zhang, Electrolyte and Interphase Engineering of Aqueous Batteries Beyond "Water-in-Salt" Strategy, *Adv. Mater.*, 2024, **36**(17), 2306508.

3 J. Deng, H. Luo, Q. Gou, J. Wang, Z. Chen, N. Xu, Z. Liu, Y. He, Z. Luogu, G. Jiang, *et al.*, Subnanocyclic Molecule of 15-Crown-5 Inhibiting Interfacial Water Decomposition and Stabilizing Zinc Anodes via Regulation of Zn2+ Solvation Shell, *J. Phys. Chem. Lett.*, 2023, **14**(41), 9167–9175.

4 C. Li, Q. Gou, R. Tang, J. Deng, K. Wang, H. Luo, J. Cui, Y. Geng, J. Xiao, Y. Zheng, *et al.*, Electrolyte Modulation of Biological Chelation Additives toward a Dendrite-Free Zn Metal Anode, *J. Phys. Chem. Lett.*, 2023, **14**(41), 9150–9158.

5 Q. Liao, K. Sun and J. Wang, A new platform for clean energy and sustainable environment in the new era of decarbonization, *DeCarbon*, 2023, **1**, 100001.

6 S. L. Zhou, A. A. Shah, P. K. Leung, X. Zhu and Q. Liao, A comprehensive review of the applications of machine learning for HVAC, *DeCarbon*, 2023, **2**, 100023.

7 Z.-Q. Wang, H.-M. Chen, X.-D. Liu, L.-Y. Song, B.-S. Zhang, Y.-G. Yang, Z.-C. Zhang, Q. Li, T.-Q. Gao, J. Bai, *et al.*, Amorphous K-Buserite Microspheres for High-Performance Aqueous Zn-Ion Batteries and Hybrid Supercapacitors, *Adv. Sci.*, 2023, **10**(13), 2207329.

8 Q. Wang, W. Zhou, Y. Zhang, H. Jin, X. Li, *et al.*, Rescue of dead MnO2 for stable electrolytic Zn–Mn redox-flow battery: a metric of mediated and catalytic kinetics, *Natl. Sci. Rev.*, 2024, **11**(8), nwae230.

9 Q. Zheng, Z. A. H. Goodwin, V. Gopalakrishnan, A. G. Hoane, M. Han, R. Zhang, N. Hawthorne, J. D. Batteas, A. A. Gewirth and R. M. Espinosa-Marzal, Water in the Electrical Double Layer of Ionic Liquids on Graphene, *ACS Nano*, 2023, **17**(10), 9347–9360.

10 S. Zhang, J. Chen, W. Chen, Y. Su, Q. Gou, R. Yuan, Z. Wang, K. Wang, W. Zhang, X. Hu, *et al.*, Regulating Water Molecules via Bioinspired Covalent Organic Framework Membranes for Zn Metal Anodes, *Angew. Chem., Int. Ed.*, 2025, **64**(14), e20244184.

11 Z. Yang, B. Wang, Y. Chen, W. Zhou, H. Li, R. Zhao, X. Li, *et al.*, Activating sulfur oxidation reaction via six-electron redox mesocrystal NiS2 for sulfur-based aqueous batteries, *Natl. Sci. Rev.*, 2023, **10**(6), nwac268.

12 S. Zhang, Q. Gou, W. Chen, H. Luo, R. Yuan, K. Wang, K. Hu, Z. Wang, C. Wang, R. Liu, *et al.*, Co-Regulating Solvation Structure and Hydrogen Bond Network via Bio-Inspired Additive for Highly Reversible Zinc Anode, *Adv. Sci.*, 2024, **11**(35), 2404968.

13 H. Schäfer, A. Schuster, S. Kunis, T. Bookholt, J. Hardege, K. Rüwe and J. Brune, The Readiness of Water Molecules to Split into Hydrogen + Oxygen: A Proposed New Aspect of Water Splitting, *Adv. Mater.*, 2023, **35**(30), 2300099.

14 D. P. Leonard, Z. Wei, G. Chen, F. Du and X. Ji, Water-in-Salt Electrolyte for Potassium-Ion Batteries, *ACS Energy Lett.*, 2018, **3**(2), 373–374.

15 C. Yang, J. Chen, T. Qing, X. Fan, W. Sun, A. von Cresce, M. S. Ding, O. Borodin, J. Vatamanu, M. A. Schroeder, *et al.*, 4.0 V Aqueous Li-Ion Batteries, *Joule*, 2017, **1**(1), 122–132.

16 Z. Luogu, Q. Gou, H. Luo, Z. Chen, J. Deng, K. Wang, Y. He, Y. Li, L. Wang, B. Zhang, *et al.*, A bio-inspired membrane of interfacial engineering in the cathode in aqueous magnesium-ion batteries, *Sci. China Mater.*, 2024, **67**(8), 2558–2566.

17 Y. Li, J. Jiang, X. Li, M. Li, Y. Zheng and K. Sun, MXenes with functional N terminal group offer a covalent bond storage mechanism for anions, *Phys. Rev. B: Condens. Matter Mater. Phys.*, 2024, **110**(15), 155401.

18 K.-X. Wang, R.-D. Yuan, Y.-T. He, S.-H. Reng, Q.-Z. Gou, S.-D. Zhang, J.-B. Deng, Z.-G. Luogu, Z.-Y. Chen, X.-X. Gu, *et al.*, Biological ion channel inspired interfacial protection layer for high-performance zinc-ion batteries, *Rare Met.*, 2024, **44**, 912–924.

19 G. Licht, K. Hofstetter and S. Licht, Separation of molten electrolyte from the graphene nanocarbon product subsequent to electrolytic CO2 capture, *DeCarbon*, 2024, **4**, 100044.

20 L. Suo, O. Borodin, T. Gao, M. Olguin, J. Ho, X. Fan, C. Luo, C. Wang and K. Xu, "Water-in-salt" electrolyte enables high-voltage aqueous lithium-ion chemistries, *Science*, 2015, **350**(6263), 938–943.

21 Q. Gou, Z. Chen, H. Luo, J. Deng, B. Zhang, N. Xu, J. Cui, Y. Zheng, M. Li and J. Li, Synergistic Modulation of Mass Transfer and Parasitic Reactions of Zn Metal Anode via Bioinspired Artificial Protection Layer, *Small*, 2024, **20**(6), 2305902.

22 T. Ye, H. Gao, Q. Li, N. Liu, X. Liu, L. Jiang and J. Gao, Highly Selective Lithium Transport through Crown Ether Pillared Angstrom Channels, *Angew. Chem., Int. Ed.*, 2024, **63**(7), e202316161.

23 T. Liu, H. Wu, H. Wang, Y. Jiao, X. Du, J. Wang, G. Fu, Y. Zhang, J. Zhao and G. Cui, A Molecular-Sieving Interphase Towards Low-Concentrated Aqueous Sodium-Ion Batteries, *Micro & Nano Lett.*, 2024, **16**(1), 144.

24 J. Zhou, M. Xie, F. Wu, Y. Mei, Y. Hao, R. Huang, G. Wei, A. Liu, L. Li and R. Chen, Ultrathin Surface Coating of Nitrogen-Doped Graphene Enables Stable Zinc Anodes for Aqueous Zinc-Ion Batteries, *Adv. Mater.*, 2021, **33**(33), 2101649.

25 B. Li, R. A. Rietmeijer and S. G. Brohawn, Structural basis for pH gating of the two-pore domain K+ channel TASK2, *Nature*, 2020, **586**(7829), 457–462.

26 H. Luo, Q. Gou, Y. Zheng, K. Wang, R. Yuan, S. Zhang, W. Fang, Z. Luogu, *et al.*, Machine Learning-Assisted High-Donor-Number Electrolyte Additive Screening toward Construction of Dendrite-Free Aqueous Zinc-Ion Batteries, *ACS Nano*, 2025, **19**(2), 2427–2443.

27 J. Deng, G. Xue, C. Li, S. Zhao, Y. Zheng, Y. He, R. Yuan, K. Wang, T. Mo, Y. Xiang, Y. Chen, Y. Geng, L. Wang, G. Feng, X. Hou and M. Li, Accelerating Ion Desolvation via Bioinspired Ion Channel Design in Nonconcentrated Aqueous Electrolytes, *J. Am. Chem. Soc.*, 2025, **147**, 5943–5954.

28 D. A. Doyle, J. M. Cabral, R. A. Pfuetzner, A. Kuo, J. M. Gulbis, S. L. Cohen, B. T. Chait and R. MacKinnon, The Structure of the Potassium Channel: Molecular Basis of K+ Conduction and Selectivity, *Science*, 1998, **280**(5360), 69–77.

29 J. Chen, B. Liu, H. Cai, S. Liu, Y. Yamauchi and S. C. Jun, Covalently Interlayer-Confined Organic–Inorganic Heterostructures for Aqueous Potassium Ion Supercapacitors, *Small*, 2023, **19**(4), 2204275.

30 J. Chen, W. Zhao, J. Jiang, X. Zhao, S. Zheng, Z. Pan and X. Yang, Challenges and perspectives of hydrogen evolution-free aqueous Zn-Ion batteries, *Energy Storage Mater.*, 2023, **59**, 102767.

31 S. Huang, X. Du, Y. Guo, Z. Liang, M. Ma, X. Sun and L. Xiong, Electrode Surface-Modified Strategy for Improving the Voltage of Aqueous Supercapacitors, *Small*, 2023, **20**(21), 2306867.

32 J. R. Bordin, A. V. Ilha, P. R. B. Côrtes, W. da Silva Oliveira, L. A. Pinheiro, E. E. de Moraes, T. G. Grison and M. H. Köhler, Molecular modeling of aquaporins and artificial transmembrane channels: a mini-review and perspective for plants, *Theor. Exp. Plant Physiol.*, 2023, **36**, 619–634.

33 S. Kavousi, B. R. Novak, X. Tong and D. Moldovan, Molecular dynamics simulation study of the positioning and dynamics of α-tocopherol in phospholipid bilayers, *Eur. Biophys. J.*, 2021, **50**(6), 889–903.

34 X. Pan, D. Xu, X. Tang, N. Liu, Y. You, X. Wang, X. Yan, X. Ma and X. Chen, Endocytosis-Enabled Construction of Silica Nanochannels Crossing Living Cell Membrane for Transmembrane Drug Transport, *Adv. Funct. Mater.*, 2020, **30**(38), 2002761.

35 T. Shigematsu, K. Koshiyama and S. Wada, Stretch-Induced Interdigitation of a Phospholipid/Cholesterol Bilayer, *J. Phys. Chem. B*, 2018, **122**(9), 2556–2563.

36 H. Amiri, K. L. Shepard, C. Nuckolls and R. Hernández Sánchez, Single-Walled Carbon Nanotubes: Mimics of Biological Ion Channels, *Nano Lett.*, 2017, **17**(2), 1204–1211.

37 C. M. Nimigean, 35 years of channelling potassium ions, *Nature*, 2022, **608**, 670–671.

38 W. Chen, Y. Wang, F. Wang, Z. Zhang, W. Li, G. Fang and F. Wang, Zinc Chemistries of Hybrid Electrolytes in Zinc Metal Batteries: From Solvent Structure to Interfaces, *Adv. Mater.*, 2024, **36**(47), 2411802.

39 Z. Li, D.-T. Nguyen, J. D. Bazak, K. S. Han, Y. Chen, V. Prabhakaran, T. T. Le, Z. Cheng, M. Song, V. G. Pol, *et al.*, Stable Cycling of Mg Metal Anodes by Regulating the Reactivity of Mg2+ Solvation Species, *Adv. Energy Mater.*, 2024, **14**(16), 2301544.

40 J. Han, A. Mariani, A. Varzi and S. Passerini, Green and low-cost acetate-based electrolytes for the highly reversible zinc anode, *J. Power Sources*, 2021, **485**, 229329.

41 T. C. Li, Y. Lim, X. L. Li, S. Luo, C. Lin, D. Fang, S. Xia, Y. Wang and H. Y. Yang, A Universal Additive Strategy to Reshape Electrolyte Solvation Structure toward Reversible Zn Storage, *Adv. Energy Mater.*, 2022, **12**(15), 2103231.

42 G. Kresse and J. Furthmüller, Efficiency of ab-initio total energy calculations for metals and semiconductors using a plane-wave basis set, *Comput. Mater. Sci.*, 1996, **6**(1), 15–50.

43 Y. Wu, Q. Hu, H. Liang, A. Wang, H. Xu, L. Wang and X. He, Electrostatic Potential as Solvent Descriptor to Enable Rational Electrolyte Design for Lithium Batteries, *Adv. Energy Mater.*, 2023, **13**(22), 2300259.

44 S. Cai, X. Chu, C. Liu, H. Lai, H. Chen, Y. Jiang, F. Guo, Z. Xu, C. Wang and C. Gao, Water–Salt Oligomers Enable Supersoluble Electrolytes for High-Performance Aqueous Batteries, *Adv. Mater.*, 2021, **33**(13), 2007470.

45 X. Tang, P. Wang, M. Bai, Z. Wang, H. Wang, M. Zhang and Y. Ma, Unveiling the Reversibility and Stability Origin of the Aqueous V2O5–Zn Batteries with a ZnCl2 "Water-in-Salt" Electrolyte, *Adv. Sci.*, 2021, **8**(23), 2102053.

46 M. Li, X. Wang, J. Meng, C. Zuo, B. Wu, C. Li, W. Sun and L. Mai, Comprehensive Understandings of Hydrogen Bond Chemistry in Aqueous Batteries, *Adv. Mater.*, 2024, **36**(3), 2308628.

47 W. Ma, S. Wang, X. Wu, W. Liu, F. Yang, S. Liu, S. C. Jun, L. Dai, Z. He and Q. Zhang, Tailoring desolvation strategies for aqueous zinc-ion batteries, *Energy Environ. Sci.*, 2024, (17), 4819–4846.

48 M. He, J. Chen, A. Hu, Z. Yan, L. Cao and J. Long, Manipulating cation-water chemistry to inhibit hydrogen evolution of zinc metal anodes, *Energy Storage Mater.*, 2023, **62**, 102941.

49 E. T. Acar, S. F. Buchsbaum, C. Combs, F. Fornasiero and Z. S. Siwy, Biomimetic potassium-selective nanopores, *Sci. Adv.*, 2019, **5**(2), 2568.

50 M. Chen, J. Wu, T. Ye, J. Ye, C. Zhao, S. Bi, J. Yan, B. Mao and G. Feng, Adding salt to expand voltage window of humid ionic liquids, *Nat. Commun.*, 2020, **11**(1), 5809.

51 K. Ge, H. Shao, E. Raymundo-Piñero, P.-L. Taberna and P. Simon, Cation desolvation-induced capacitance enhancement in reduced graphene oxide (rGO), *Nat. Commun.*, 2024, **15**(1), 1935.

52 K. Wang, Y. He, R. Yuan, Q. Gou, S. Zhang, H. Mei, Y. Zheng, J. Wang and M. Li, A bioimmune mechanism-inspired targeted elimination mechanism on the anode interface for zinc–iodine batteries, *Chem. Sci.*, 2025, **16**, 7227–7238.